Scaling and Experimental Studies of Condensation Oscillation in Subcooled Water of the In-containment Refueling Water Storage Tank

Jun Hyung Lee and Hee Cheon No
Korea Advanced Institute of Science and Technology

Abstract

Condensation oscillation by jetting the steam into subcooled water through spargers is studied. To provide the suitable guideline for the verification experiment of the IRWST in the next generation reactor, scaling methodology has been introduced and is verified by experiments within the possible range of operating and physical parameters. The dominant scaling parameters related to its pressure oscillation are also verified. The volumetric effects of the system and the different dynamic characteristics between the shell side and the bottom plate are also investigated. Two types of condensation oscillations are identified. The test facility has been set up according to the scaling methodology. The test results show that the pressure amplitudes are dependent on the mass flux, the shapes of spargers, the subcooling, and the volume of the system as shown in the scaling methodology. It is concluded that the well-designed spargers greatly reduce the pressure amplitudes, that by the scaling methodology the effects of the system volume can be estimated, and that the bottom plate is apt to be a weak spot under the pressure pulsation due to condensation oscillation.

1. Introduction

Center for Advanced Reactor Research (CARR) has developed a passive PWR concept called CARR Passive Reactor 1300Mwe (CP-1300) since 1991. CP-1300 has the same Reactor Coolant System (RCS) configuration as Korea Next Generation Reactor (KNGR). Among the several passive safety features, there is an In-Containment Refueling Water Storage Tank, called IRWST. At the event of Total Loss of Feedwater (TLOFW), continued steam blowdown gives severe pressure pulsations at a certain subcooling ; imposing those loads on the IRWST boundaries. Direct contact condensation in subcooled liquid is a common phenomenon encountered in many two-phase systems. For studying of the steam condensing phenomena, the experimental approaches rather than the analytical ones have been preferred. The pressure amplitudes, due to those condensations, are seen to grow with the pool bulk temperature to a certain value but show rapid decrease thereafter. When the pressure amplitude becomes maximum, severe oscillation loads are imposed on the pool boundaries. Several related incidents were reported in NUREG-0783. The guidelines presented in NUREG-0783 are applicable to the suppression pool of a BWR plant. According to the changes of the operating and physical parameters, the reevaluation of the guidelines, suggested

in NUREG-0783, is necessary. As the anticipated mass fluxes for the accident scenario are not in the chugging mode but in the condensation oscillation mode, the considerations of the low steam fluxes can be ruled out.

Claudio Damasio (1985) provided the dimensionless groups for condensation frequencies via Jacob numbers, Reynolds numbers, and Weber numbers. According to his results, the frequencies increase as the steam mass flux increases; At intermediate and high steam flow rates, the condensation frequencies decrease as the water subcooling decreases. Water temperature and steam mass flux being equal, frequency decreases as the discharge tube diameter increases. Izuo AYA et al (1983) also mentioned similar frequency variations and considered the effects of the volume of system.

Jung-hoon CHUN (1983) found out the condensation instabilities with various discharge nozzle shapes and mass fluxes up to 500 Kg/s m^2. As studied by Kerney et al. (1972), the sizes of the steam cavities grow as the subcooling decreases. An increase of the subcooling and the translatory motions enhance heat transfer rate, causing a shorter collapse time. The maximum loads may have occurred at a 'finite' subcooling due to the facts that the necessary conditions require low enough subcooling to have a large bubble and high enough subcooling to have a short collapse time. Motoaki UTAMURA (1986) exceptionally provided the experimental correlations for the pressure amplitudes via dimensionless subcooling.

According to the magnitudes of steam mass fluxes, the condensation phenomena in low mass flux are different from those in high mass flux. At low mass fluxes, discharged steam diverges out whereas the steam cavity is formed at high mass fluxes. The higher the mass fluxes, the lower the pressure pulsation. However the previous tests for condensation oscillations did not clearly define the fact that the steam cavity is not formed when the steam mass flux becomes lower than that of the sonic flow. Figures 1 and 2 show the different condensation phenomena. In the cylindrical-diverging jet (Figure 1), the momentum force of ejected steam is not sufficient for forming the steam cavity and the broken bubbles diverge into the subcooled water. Whereas the other one as shown in Figure 2, the momentum force of ejected steam is sufficient for forming the steam cavity. The steam cavity is formed and is tapered to discharge tiny bubbles at the apices called "tip streaming". Regarding the pressure pulsations between those two types of condensations, Type I condensation, as shown in Figure 1, gives higher pressure peaks up to a certain subcooling. In the actual operation of the IRWST, two kinds of events are also predicted. Two different kinds of condensation oscillations should be identified and be quantified via the region of condensation and the pressure amplitudes.

This study is 1) to develope the scaling methodology for setting up the test facility simulating the prototype, 2) to find out the scaling parameters affecting the unstable condensations, 3) and to experimentally demonstrate which scaling parameters are dominant.

2. Scaling Methodology

Figure 3 shows the scaling procedure of scaling methodology. Since there is no energy change up to the steam exit region, only the mass balance equation is used. The similarity

requirement for the scaling methodology becomes

$$\phi_R = \frac{\phi_m}{\phi_p} = \frac{\phi \ \ for \ \ model}{\phi \ \ for \ \ prototype} \tag{1}$$

2.1 Mass Conservation

The followings are the nondimensionalized mass conservation equations at each region. Figure 4 shows the schematic diagram of mass conservation.

o Steam Generating Region : $\quad N_{rd} \cdot \dfrac{d(\rho_v^+ V_v^+)}{dt^+} = - W_{v \ in}^+ + \dfrac{Q_{input}^+}{h_{fg}^+}$ (2)

with the following nondimensional variables :

$$W_{v \ in}^* = \frac{W_{v \ in}}{W_0} \ , \ \ Q_{input}^* = \frac{Q_{input}}{Q_{input \ o}} \ , \ \ h_{fg}^* = \frac{h_{fg}}{h_{fgo}}$$

$$\rho_v^* = \frac{\rho_v}{\rho_{vo}} \ , \ \ V_v^* = \frac{V_v}{V_d} \ , \ \ t^* = \frac{t}{\tau_o}$$

The other regions can be nondimensionalized as the same procedure.

o Pipe Run Region : $\quad N_{rb} \cdot \dfrac{d(\rho_v^+ V_v^+)}{dt^+} = W_{v \ in}^+ - W_{v \ out}^+$ (3)

o Steam Condensation Region : $\quad N_{rb} \cdot \dfrac{\rho_{vb}^+ V_{vb}^+}{dt^+} = \dfrac{W_{v \ out}^+}{N_{perforated \ holes} N_{spargers}} - W_c^+$ (4)

o Overall Mass Conservation : $\quad \dfrac{(\rho V)_0}{\tau_0 \ W_0} \ \sum_j \dfrac{d(\rho V)_j^+}{dt^+} \ = \ W_{source}^+ - N_{spargers} W_c^+$ (5)

2.2 Integral Momentum Equation

The integral momentum equation from the steam generating region to the condensation region can be set up as follows:

$$\frac{d(\rho v V)_s}{dt} + [(A \rho v^2)_s]_{in}^{out} + A[p]_{in}^{out} = \int_{V_i} (\Gamma v_i - F_i - F_w) dV \tag{6}$$

Nondimensionalized form becomes

$$(\frac{I W_0}{\tau_{mom} \rho_0 v_{L0}^2}) \cdot \frac{\tau_{mom}}{\tau_0} \cdot \frac{d W_v^+}{dt^+} + [\frac{W_b^{+2}}{\rho_v^+ A_f^{+2}}]_{in}^{out} + \frac{\delta p_0}{(\rho v^2)_{L0}} [p^+]_{in}^{out}$$

$$= -[\sum_j \frac{f_j L_j}{D_{hj}} + \sum_k K_k] \frac{(\rho v^2)^+ L}{2} - f_i \cdot \frac{\rho_v^+ \overline{v_{ib}^{+2}}}{2} + \frac{W_c^+ v_i^+}{A_f^+} \tag{7}$$

$[\sum_j \dfrac{f_j L_j}{D_{hj}} + \sum_k K_k] = 1$: frictional requirement

$I_R = (\sum_j \dfrac{L_{jo}}{A_{jo}})_R = (\dfrac{L_o}{A_o})_R = 1$: dynamic similarity automatically satisfied

$[\tau_{mom}]_R = [\dfrac{I W_o}{\rho v_{Lo}^2}]_R = 1$: from momentum similarity

$$[N_{\tau\,mom}]_R = [\frac{\tau_{mom}}{\tau_0}]_R = [\frac{(\frac{IV_0}{v_0^2})}{(\frac{\rho_0 V_0}{W_0})}]_R = 1$$

$$[\delta p_0]_R = [p_{D0} - p_{pool\,gas}]_R = 1 \rightarrow [p_{D0}]_R = 1 \quad if\ [p_{pool\,gas}]_R = 1$$

2.3 Bubble Momentum Equation

The nondimensionalized bubble momentum equation from the Rayleigh bubble equation was set up, considering the scaling effects of frictional loss term, shape factor and submergence effect:

$$\frac{\rho_f V_{b0}^{2/3}}{\tau_b^2 \rho_0 v_0^2}[\frac{d^2 R_b^+}{dt^{+2}} + \frac{3}{2} \cdot (\frac{dR_b^+}{dt^+})^2]$$

$$= \frac{\delta p_0}{(\rho v^2)_0}[p_D - p_i] + \frac{\rho_f\, g\, L_{s0}}{(\rho v^2)_0} \cdot (H_i^+ - z^+) - (\frac{fL}{D_h} + K)\frac{\rho_b^+ v_b^{+2}}{2} \tag{8}$$

where $\quad \tau_b = (\frac{\rho_f}{\rho_g})^{\frac{1}{2}} \frac{V_{b0}^{\frac{1}{3}}}{v_o}$, and $\quad N_{\tau\,bubble} = (\frac{\rho_f}{\rho_g})^{\frac{1}{2}} \cdot (\frac{V_{b0}^{\frac{1}{3}}}{L_o})$

2.4 Energy Equation

We can write the energy equation for the pool as

$$\frac{\rho_{pool} V_{pool}}{W_0\, \tau_{pool}} \cdot \frac{\tau_{pool}}{\tau_0} \frac{d(e_{pool}^+)}{dt^+} = W_c^+ h_{fg}^+ - W_{i\,evap}^+ h_{fg}^+ - \frac{Q_w}{W_0 \Delta h_0} \tag{9}$$

where the left hand side of the last two terms represent evaporative losses and heat losses of the pool tank, respectively.

$$[\tau_{pool}]_R = [\frac{\rho_{pool} V_{pool}}{W_o}]_R = 1$$

$$[N_{\tau\,pool}]_R = [\frac{\tau_{pool}}{\tau_o}]_R = [\frac{\rho_p V_p}{\rho_o V_o}]_R = [\frac{M_p}{M_o}]_R = 1$$

The final scaling methodology and parameters are presented in Table 1.

2.5 Linear Analysis for Volume Perturbation

The volume perturbation of the condensation oscillation can be simulated. It is assumed that liquid inertia is represented by a virtual mass attached to the control volume. Formal generalization of the Rayleigh equation gives

$$\delta p = m_0 \frac{d^2 \delta V}{dt^2} \tag{10}$$

where $\quad m_o \equiv \rho_l V^{-1/3} \frac{3}{(4\pi)^2}$

The pool momentum equation, bulk modulus of steam, and Clapeyron-Clausius relation, were also incorporated into the mass conservation equation.

$$\frac{d(\rho V)}{dt} = \rho A u - \frac{h \Delta T \varepsilon V}{h_{fg}} \tag{11}$$

The nondimensionalized linear equation of volume perturbation for condensation oscillation can be set as follows:

$$\frac{d^3 \delta V^*}{dt^{*3}} + \left[\frac{C^2 \varepsilon h T_{sat} L_0}{\rho h_{fg}^2 u_0} - \frac{M^2}{K_f} - 1 \right] \cdot \frac{d^2 \delta V^*}{dt^{*2}} + M^2 \cdot \frac{\rho L_0^2}{m_0 V_0} \cdot \frac{d \delta V^*}{dt^*} + M^2 \cdot \frac{L_0^3}{u_0} \frac{\varepsilon h \delta T}{m_0 V_0 h_{fg}} \cdot \delta V^* = 0 \tag{12}$$

where M represents Mach number and ε is the multiplication factor for extraneous heat transfer areas. Figure 4 represents the effects of discharge diameters and thermal plume length for the frequencies of condensation oscillation.

3. Experimental Work

The experimental apparatus used is shown in Fig. 4.1. The electrically heated steam generator yields saturated steam at a pressure of 300 kPa approximately. The steam generator is controlled by steam temperature. In this experiment, the temperature of the steam generator is maintained by about 130℃ during the experiments. The steam flow rate is measured by means of pneumatic actuated control valve. Before steam flow is supplied into the test section, a moisture separator is installed to remove the suspended liquid droplets. So, it is possible to make steam flow in a saturation condition. The piezoelectric pressure transducers are equipped to measure the pressure pulsations at the side wall and at the bottom plate of the pool tank. They are flush-mounted on each sides of the pool. A PCB Piezoelectronics Model 106B is used. These are high sensitivity, acceleration compensated ICP quartz pressure sensors suitable for measuring low pressure acoustic phenomena in hydraulic and pneumatic system. They have the unique capability to measure small pressure changes of less than 0.001 psi under high static conditions. Also the sensitivity is 300mV/psi and a resolution of 91dB (0.0001 psi). The measurement of the temperatures is accomplished by T-type thermocouples. To measure the bulk temperature, 4 thermocouples were inserted into the pool with 50 mm depth. And the temperature profile of the thermal plume is measured by using the instrumented bar represented in Fig. 4.2. Dynamic characteristics of the pool tank is also important to assure the structural integrity of the pool. Dynamic characteristics of the pool was measured by an accelerometer and an impact hammer. The first natural frequencies were 91 Hz at side wall and 101 Hz at bottom plate. This tells that the response pressures of the bottom plate are slightly greater than those of the side wall.

3.1 Test Facility

Figure 5 shows the test facility. Axial temperature profiles were also measured by 10 thermocouples linearly mounted on the instrument bar.

3.2 Test Matrix
o Operating Parameters

Mass flux, Kg/m²s	Pool subcooling(△T), K
70, 100, 150, 200, 300	from 20 to 70

o *Physical Parameters*

Hole diameters	Number of holes / orientation	Pool size	Volume of upstream
26.64 mm (1") 15.80 mm (1/2") 10 mm 5 mm	Single / Multiple Horizontal/Vertical	Pressure variations with different pool sizes	S/G region Pipe run region Header volume

3.3 Bubble Breakup

Hinze (1955) represented the basic type of bubble deformations. The main cause of the deformations are external dynamic pressures and viscous stresses. Three forces per unit area control the deformation/breakup of bubbles and are grouped into two dimensionless parameters , a generalized Weber group and a viscosity group:

$$N_{We} = \frac{\tau D}{\sigma}, \quad N_{vi} = \frac{\mu_d}{\sqrt{\rho_d \sigma D}} \tag{13}$$

where τ ($= \rho u^2$) represents the momentum flow around the bubble, and subscript d and D mean the dispersed phase and the diameter of bubble, respectively. As shown in equation (13), the momentum of the flow is the governing factor to break the bubble. The breakup of the bubbles is always present when the Weber number of the flow exceeds the critical values (Hinze, 1955). It is concluded that the boundary conditions of the bubbles control the breakup and the dispersion of the bubbles. The ejected steam agitates the surrounding fluid and makes it turbulent. This kind of fluid conditions is enough to make a bubble break into smaller ones. Regarding the final sizes of bubbles, several correlations have been introduced with relation to the turbulent intensity of surrounding fluid. S. M. Bhavaraju (1978) showed that the steam Reynolds number ($Re = \frac{U_{steam} D \, \rho_{steam}}{\mu_{steam}}$) exceeds the critical value ($Re > 10,000$), the ejected bubble diameters to be weakly dependent on the mass fluxes and on the diameters of the exit holes. The bubble size reaches eventually an asymptotic value due to the velocity of the steam. The steam Reynolds numbers, relating to the tests of the steam condensation, are far beyond those values. The dispersing bubbles are very small in size regardless the type of condensations. Furthermore the condensation makes it very tiny bubbles. The appearance of the tiny bubbles is very close to the exit holes in Type I condensation and near the steam cavity boundaries in Type II condensation. It is concluded

that the ejected steam has been condensed near the exit holes. It is very hard to discern the boundaries of condensation.

3.4 Test Results

Figure 7 shows the difference of the pressure peaks with different mass fluxes. The pressure amplitudes of Type I condensation are larger than those of Type II condensation up to a certain subcooling. This fact tells that the volume of the system affects the condensation phenomenon. If the mass fluxes exceed 200 kg/m^{2}s, then the pressure amplitudes becomes lower. The subcooling resulting in the maximum pressure amplitudes is about 20 ℃ regardless of the mass fluxes. Figure 8 shows the comparisons of the condensation frequencies with existing correlations. The longer the condensation periods due to the decrease of the subcooling, the smaller the condensation frequencies. The first natural frequency of the tank is lower than that of the condensation frequencies so the failure of the pool tank due to resonance can be excluded. Figure 9 shows the temperature profiles and the pressure peaks. The temperatures were measured axially from the exit spot of the holes to the distance up to 180mm. The bulk temperatures are designated as T_b. The differences of the temperatures between the bulk and the axial become narrower according to the decrease of subcooling. The temperature suddenly decreases at 20 mm of the axial positions. This tells that the condensation regions are located mainly within 20 mm and that the effects of the bubble dispersion and the turbulence cause the differences between the bulk and the local temperatures. From the pressure-temperature curves, the maximum subcooling resulting in the maximum pressure amplitudes is 20 ℃. Figure 10 shows that the maximum pressure amplitude becomes one-fourth as the diameter of the discharge hole becomes half. Table 2 shows the scaling relation between 5 mm and 10 mm discharge holes. The ratio of numbers from the integral momentum equation also becomes one-fourth. From this fact, the scaling number clearly reflects the volumetric change of steam cavity and the discharge area.

Figure 11 shows the effects of the multiple holes sparger. The multiple holes sparger is made up of two 10mm holes facing the side of the pool and one 7 mm hole facing downward. One on the right hand side of Figure 11 shows the case of the multiple holes sparger. The pressure amplitudes decrease slightly in case of the multiple holes sparger. Even if the total amount of steam in the side direction is larger than that in the bottom direction, the pressure amplitude at the bottom plate is higher than that at the side wall. It is concluded that the rigidity of the bottom plate is larger than that of the side wall as shown in the resonance test, and that several accidents reported in NUREG-0783 had occurred mainly at the bottom plate of the suppression pool. One way to assure the structural integrity of the pool tank is to avoid installing the internal structure in the bottom plate.

4. Conclusions

The mechanism of condensation oscillation was studied experimentally based on the scaling methodology. Some of the important parameters for the unstable condensation phenomena have been found. The primary conclusions are as follow:

(1) By the scaling methodology, the model of the test facility for condensation oscillation can be established.

(2) According to the mass fluxes, the condensation phenomena at large subcooling are grouped into two. One is the formation of steam cavity and the other is the diverging jet of steam. The pressure amplitudes become larger in case of the diverging jet of steam within certain subcooling. As the subcooling decreases, the pressure amplitudes are apparently dependent on the mass fluxes.

(3) Pressure peaks are proportional to the mass fluxes and discharge diameter, and are inversely proportional to the subcooling. The multiple holes sparger reduces the pressure amplitudes.

(4) The sizes of the broken bubbles are not dependent on the diameters of the exit pipes during the test.

(5) The pressure amplitude at the bottom plate is higher than that at the side wall.

References

1. T. M. Su, Suppression-Pool Temperature Limits for BWR Containments, NUREG-0783, 1981

2. Claudio Damasio, et al., Experimental Study on the Unstable Direct Contact Condensation Regimes, Proc. of Topical Mtg on Reactor Thermal Hydraulics, October, 1985

3. C. K. Chan & C. K. B. Lee, A Regime Map for Direct Contact Condensation, Int J. Multiphase Flow, Vol. 8, No. 1, pp. 11-20, 1982

4. S. Fukuda, Pressure Variations due to Vapor Condensation in Liquid,(II) Phenomena at Larger Vapor Mass Flow Flux, J. of JNS, Vol.24, No. 6, pp. 466-474, 1982

5. Jung-Hoon Chun, Scaling Laws & Rate Correlations for Steam Condensation on Turbulent Water, MIT dissertation, 1983

6. Motoaki UTAMURA, Pressure Oscillation Accompanying Steam Discharge into Subcooled Liquid Pool, Bulletin of JSME, Vol. 29, No. 258, 1986

7. Izuo AYA et al., Pressure and Fluid Oscillations in Vent System due to Steam Condensation, (I), J. of Nuclear Science and Technology, Vol. 17, pp. 499-515, 1980

8. Giovanni Del Tin et al, Pressure and Temperature Measurements in a Vapor Condensing Jet, Proc.7th Int .Heat Transfer Conference Munchen, Vol. 5, pp. 395-399, 1978

9. J. O. Hinze, Fundamentals of the Hydrodynamic Mechanism of splitting in Dispersion Processes, AIChE Journal, Vol. 1, No. 3, pp. 289-295, 1955

10. K. IDOGAWA et al., Formation and Flow of Gas Bubbles in a Pressurized Bubble Column with a single orifice or Nozzle Gas Distributor, Chem. Eng. Comm, Vol.59, pp. 201-212, 1987

11. S. M. Bhavaraju et al., The Design of Gas Sparged Devices for Viscous Liquid Systems, AIChE Journal, Vol. 24, No. 3, pp. 454-466, 1978
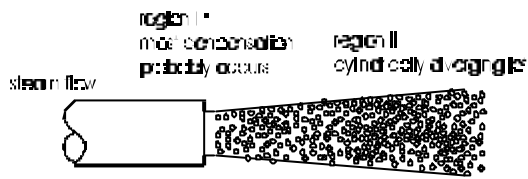
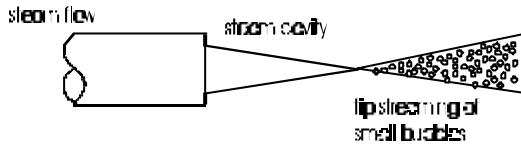Figure 1. Cylindrically diverging jet (Type I condensation)

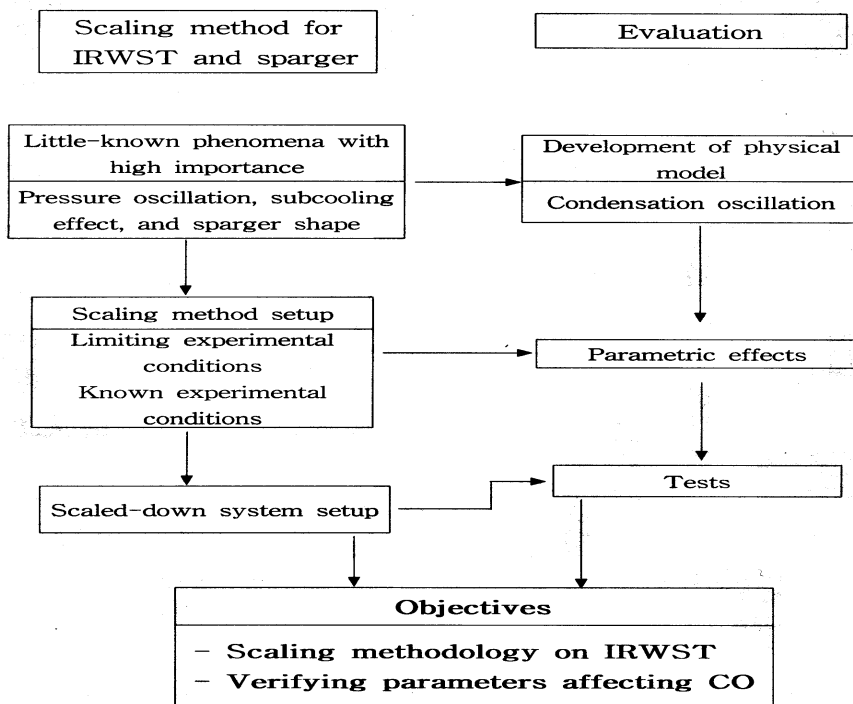Figure 2. Steam cavity and tip streaming (Type II condensation)
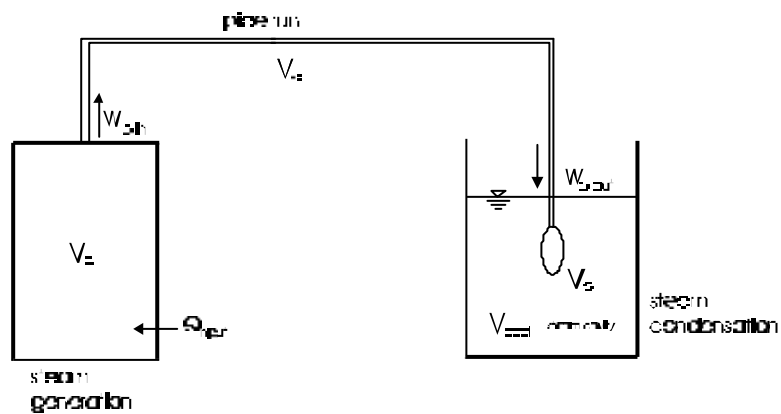

Figure 3. Scaling process

Figure 4. Schematic diagram of system for scaling analysis

| Equation	Item	Time constant	Nondimensional parameters	Numbers acquired	Similarity requirements
Mass	Dome	$\tau_d = \dfrac{\rho_{t0} V_d}{W_d}$	$N_{\tau d} = \dfrac{\tau_d}{\tau_0}$	$\dfrac{1}{N_{sparger} \cdot N_{pipe\ run}} \cdot \dfrac{V_d}{V_b}$	$\tau_o = \dfrac{\rho_{t0} V_o}{W_o}$
	Pipe run	$\tau_p = \dfrac{\rho_{t0} V_p}{W_p}$	$N_{\tau p} = \dfrac{\tau_p}{\tau_0}$	$\dfrac{1}{N_{sparger}} \cdot \dfrac{V_p}{V_b}$	
	Hole exit	$\tau_b = \dfrac{\rho_{t0} V_b}{W_b}$	$N_{\tau b} = \dfrac{\tau_b}{\tau_0}$	1	$V_o = V_b = 4.19 \times 10^{-6} m^3$
Momentum	Integral	$\tau_{mom} = \dfrac{I W_o}{\rho v_{Lo}^2}$	$N_{\tau mom} = \dfrac{\tau_{mom}}{\tau_0}$	$\dfrac{A^2 I}{V_b}$	$[\delta P_0]_R = [P_{gas} - P_{pool}]_R = 1$ $[\Sigma \frac{fL}{D} + \Sigma K_s]_R = 1$
	Bubbling	$\tau_b = (\dfrac{\rho_f}{\rho_g})^{\frac{1}{2}} \dfrac{V_{bo}^{\frac{1}{3}}}{v_o}$	$N_{\tau bubble} = (\dfrac{\rho_f}{\rho_g})^{\frac{1}{2}} \cdot (\dfrac{V_b^{\frac{1}{3}}}{L_o})$	$\dfrac{(\dfrac{\rho_f}{\rho_g})^{1/2}(V_b^{-2/3})}{A}$	$[N_{bv}]_R = [\rho_f g L_{z0}/(\rho v^2)_0]_R = 1$ $[N_p]_R = [\delta p_0/(\rho v^2)_0]_R = 1$ $[\Sigma \frac{fL}{D} + \Sigma K_s]_R = 1$
Energy	Pool	$\tau_{pool} = \dfrac{\rho_{pool} V_{pool}}{W_o}$	$N_{\tau pool} = \dfrac{\tau_{pool}}{\tau_0}$	$\dfrac{1}{N_{sparger} \cdot N_{pipe\ run}} \cdot \dfrac{\rho_b V_d}{\rho_o V_b}$	$[\dfrac{Q_w}{W_0 \Delta h_0}]_R = 1$

Table 1. Scaling table
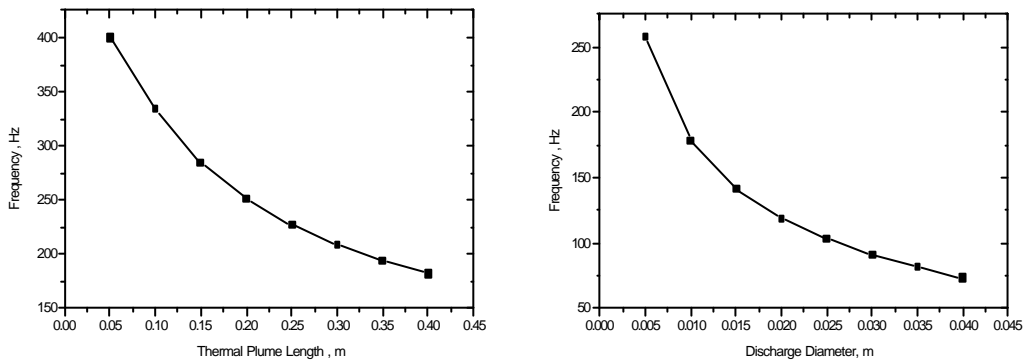
Figure 5. Frequency variations with thermal plume length and discharge diameter
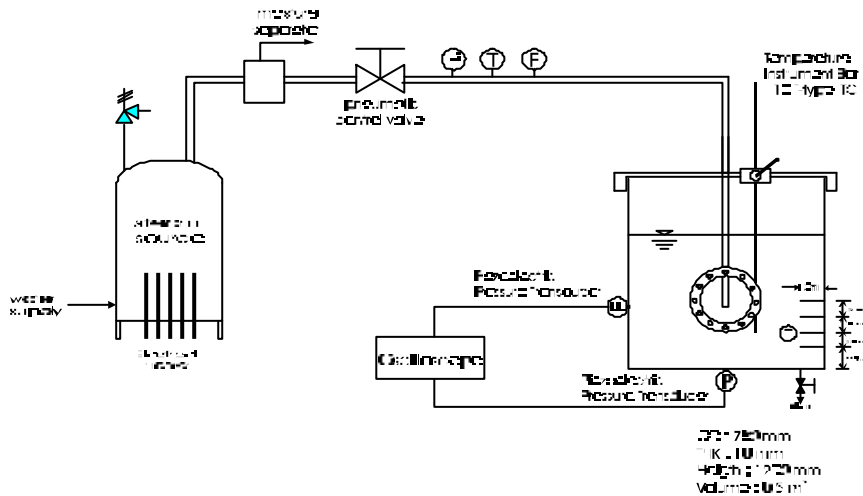

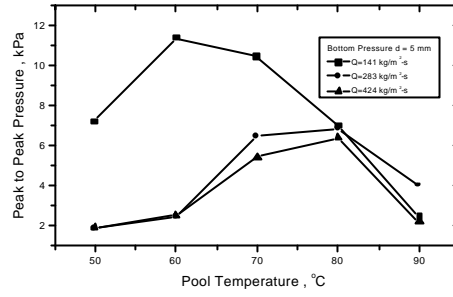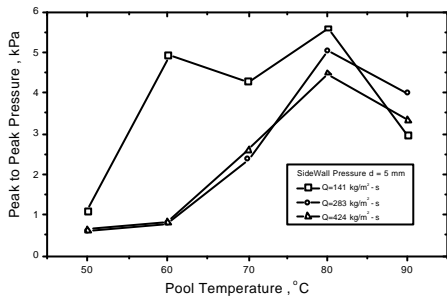Figure 6. Schematic diagram of experimental apparatus

Figure 7. Pressure amplitudes between Type I and Type II condensations
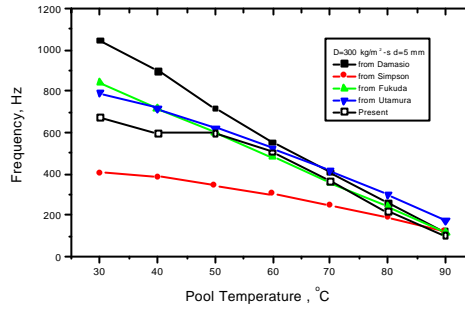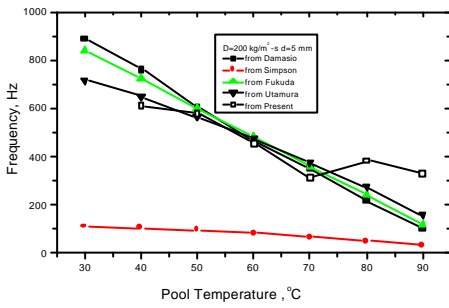(Type I: 141 kg/m²sec, Type II: 283 kg/m²sec, 424 kg/m²sec)

Figure 8. Comparison of frequencies of pressure oscillation from the present experimental
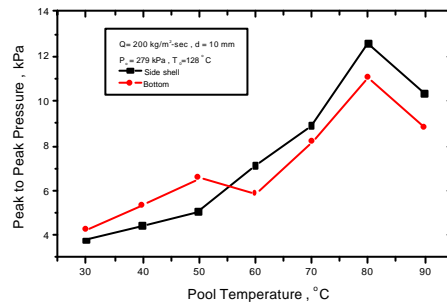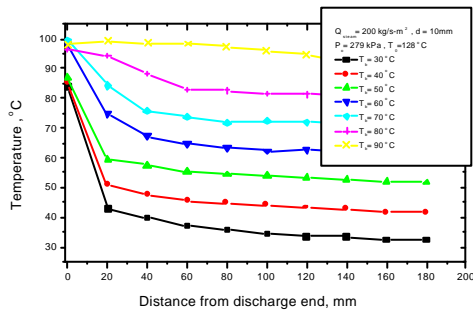data and the existing correlations

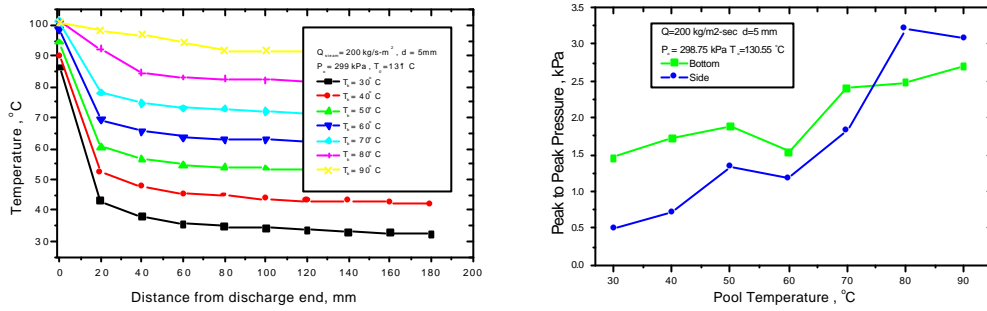Figure 9. Temperature profile and pressure peaks at Q = 200 kg/m²-sec, 10 mm pipe

Figure 10. Temperature profile and pressure peaks at Q = 200 kg/m²-sec, 5 mm pipe

Hole diameter (mm)	Area (m²)	Averaged pressure peak (kPa)	Cavity volume (m³)	Number from scaling $\frac{A^2 l}{V_b}$
5	1.964×10^{-5}	2.9	3.8×10^{-8}	1.2×10^{5}
10	7.854×10^{-5}	11.8	1.53×10^{-7}	4.76×10^{5}

Table 2. Scaling relation for pressure peaks and discharge hole diameters

Single-hole sparger

Multiple-holes sparger
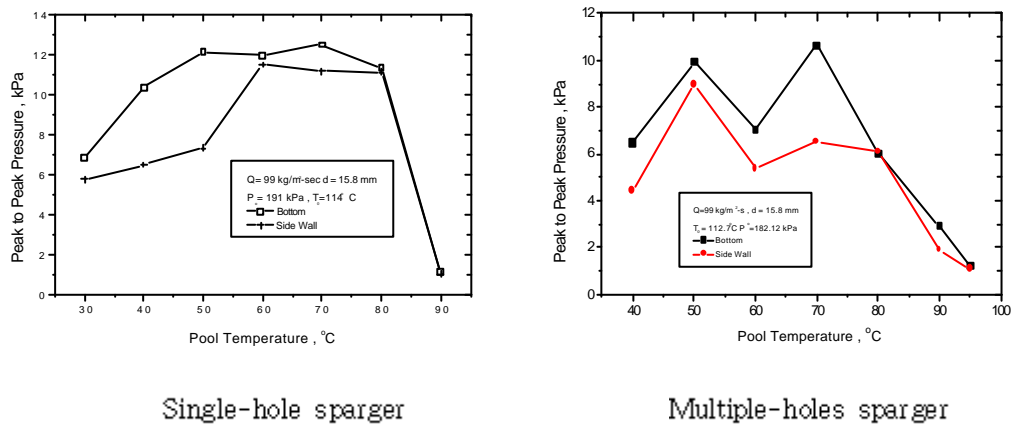
Figure 11. Comparison of pressure amplitudes between single-hole and multiple-holes sparger (2-Φ10mm and 1-Φ7mm)